Increasing strength properties in sinter-based additive manufacturing of SS316L via metal material jetting of sub-micron powders

Buhari Ibrahim[1], Lucero Lopez[2], Sohum Kulkarni[1], Dillon Jobes[1], Mattia Forgiarini[3], James R. Barber[1], Jerard V. Gordon[1,2*]

[1] Department of Mechanical Engineering, University of Michigan, Ann Arbor MI, 48109

[2] Department of Materials Science and Engineering, University of Michigan, Ann Arbor, MI 48109

[3] Azoth, 1099 Highland Dr Suite F, Ann Arbor, MI 48108

* Corresponding author: Dr. Jerard Gordon
Email addresses: jerardvg@umich.edu

Abstract

Metal Binder Jetting (MBJ) 3D printing is an attractive additive manufacturing (AM) method for high volume production of metals and ceramics. However, the widespread use of MBJ has been stymied by longstanding challenges in reduced strength properties compared with traditional wrought and laser-based AM materials. In this study, we leveraged novel "drop-on-demand" Metal Material Jetting (MMJ) of sub-micron powders to fabricate SS316L samples. These samples were subjected to dilatometry, mechanical testing, and correlative materials characterization and compared to metal binder jet (MBJ) SS316L to evaluate differences in process-structure-property relationships between the two processes. Overall, MMJ SS316L possessed an average tensile yield and ultimate tensile strength of 312 ± 84 MPa and 640 ± 38 MPa respectively, greatly exceeding MBJ SS316L in the literature due to the formation of fine microstructures with an average grain size of 2.4μm. Importantly this led to significant Hall-Petch strengthening but also considerably lower average failure strains (15.5 ± 4.8%). The process-microstructure-property relationships facilitating microstructural evolution in MMJ are discussed and further elucidated using an isotropic pressure-less viscous sintering model. Results of this model show that, although densification behaviors in MMJ were largely similar to those in MBJ, MMJ samples possessed over three-fold increase in sintering stress, defined the change in free surface energy with respect

to the volumetric shrinkage, and ~31% reduction in grain growth due to the employment of sub-micron size powders. Overall, these results show the promise of MMJ AM for structural metals and suggest that both microstructure (and ultimately strength) of MMJ materials can be further tuned by controlling the overall sintering process.

Keywords: Additive manufacturing; metal binder jetting; nanoparticles; metal material jetting; microstructure; sintering

1. Introduction

Metal Binder Jetting (MBJ) 3D printing of metals and ceramics is an attractive additive manufacturing (AM) method for high volume production. Compared with laser and electron-beam methods, MBJ offers higher speeds, increased material flexibility, and sustainability advantages [1,2]. Additionally, MBJ materials do not experience laser-processing related defects such as high residual stresses, textured microstructures, or solidification cracking [3]. However, the widespread use of MBJ has been stymied by longstanding challenges in controlling bulk defects including porosity, shrinkage, and low strength all of which negatively influence overall mechanical properties. For example, many Fe-based materials and structures fabricated by MBJ can experience part shrinkage >20%, volumetric porosity >5%, and yield strengths < 200 MPa [4–6], all of which are significant disadvantages in part production compared with traditional and laser-based AM processing of structural metals.

Defects in MBJ are intimately linked to post-processing solid state or liquid phase sintering treatments that densify green powder compacts into fully dense bodies. Generally, higher green densities are correlated with lower amounts of part shrinkage during sintering and reduced bulk porosity in the final part [4,7]. However, due to the required powder size between ~5 – 25 μm and physics of spherical powder packing, MBJ materials typically experience green part densities limited to ~50%, depending on the specific material and processing parameters utilized [1].

Common methods to enhance green part density in MBJ that have been investigated include nanoparticle additions, multimodal powder size distributions, or reactive binders, amongst others [7–9]. Overall, these methods have shown some effectiveness in increasing green density and consequently increasing densification during sintering, however, they have not been sufficient to significantly mitigate the coarse porosity typical of sintered artifacts fabricated from coarse powders. A consequence of this is that MBJ materials are generally substantially weaker than companion wrought or laser-processed AM metals [2].

Recent advances in "drop-on-demand" sinter-based AM leveraging metal material jetting (also known as "nanoparticle jetting") show promise to achieve both reduced shrinkage/porosity and higher strength properties [10,11]. Compared to MBJ, metal material jetting (MMJ) employs sub-micron powders suspended within a liquid ink carrier that is jetted into layers less than 10 μm thick. The use of sub-micron powders results in a substantially increased surface area and thus surface energy, which is the key driving force for sintering. Sub-micron powders also offer reduced sintering temperatures [12], thus reducing the potential for both shrinkage and distortion and limiting overall grain growth, all of which are significant advantages compared to MBJ and other sintering based technologies. However, as MMJ is still in its infancy compared with MBJ, understanding process-structure-property relationships is critical to achieving high-quality final materials and components.

In this study, we leveraged MMJ of a representative structural materials alloy, stainless steel 316L (SS316L) to develop new knowledge on the process-structure-property relationships for MMJ. Unlike MBJ, the sintering relationships for 3D powder compacts of sub-micron powders are largely unknown [13,14]. For example, it is well-known that sintering mechanisms at the nanoscale fundamentally differ from those of micron-scale powders due to the size dependence on

melting temperature and increase surface area [15–17]. However, sintering data on compacts made of sub-micron powders in the hundreds of nm length scale (e.g., powder sizes that MMJ processes typically employ) is lacking. Additionally, an understanding of sintering-microstructure relationships for MMJ is still lacking. To the author's best knowledge, the characterization of mechanical properties and their connection to resultant microstructure has not been undertaken for MMJ of metal alloys. Therefore, the overall goal of this study is to develop important process-structure-property relationships for MMJ as a promising AM method for production of structural alloys.

2. Materials and Methods

2.1 Sample fabrication

MMJ green samples, consisting in a mixture of metal nanopowder and held together in a defined shape by the binding agent, with geometry 9.40 mm × 9.60 mm × 5.84 mm, were fabricated on an XJET CARMEL 1400 (Revoth, Israel) using SS316L powders using an powder size of D_{50} = 0.75μm (**Figure 1a**) [18]. During printing, a proprietary solvent-dispersed metal nanoparticle solution, also referred as build ink, and proprietary soluble solid dispersion referred as support ink (Patent #: 11623280, Assignee: XJET LTD) are jetted from separate printheads [10]. A schematic of the MMJ process is shown in **Figure 1b**. The dual-material approach precisely controls the jetted area perimeter, with the support material creating a mini-vat around the layered under print. A mounted heating lamp with halogen bulbs and the hot building tray (the base substrate on which the dual-material is jetted) create a 180°C high-temperature atmosphere that evaporates the liquid and crosslinks the dissolved polymer to form a binder, which forms a thin coating that serves as bonding agent between the metal particles. After the carrier-liquid evaporates and the particles are bind together, a fine layers of metal nanoparticle agglomeration referred as print layer is created.

To level the newly printed layer at a constant height, a roller mills the top surface of each layer. The print plate indexes vertically to prepare for the next layer, and the process repeats layer by layer.

Solidified support ink supports printed objects inside the build box. The objects at this point are still in the green state with powder held together in defined shapes by the binder. Once the printjob is completed, the build plate is taken from the printer and soaked in several citric acid and water solutions to breakdown the support material and release the green parts. The green objects are then placed on ceramic plates, and thermally debinded in air atmosphere. Parts in this state are referred as brown state. It is important to know that, during the binder burn off, not all the binder evaporates and hence could affect the mechanical properties of the material, the effect of which is still being investigated. Finally, the parts are sintered and densified in a dedicated sintering furnace in hydrogen atmosphere.

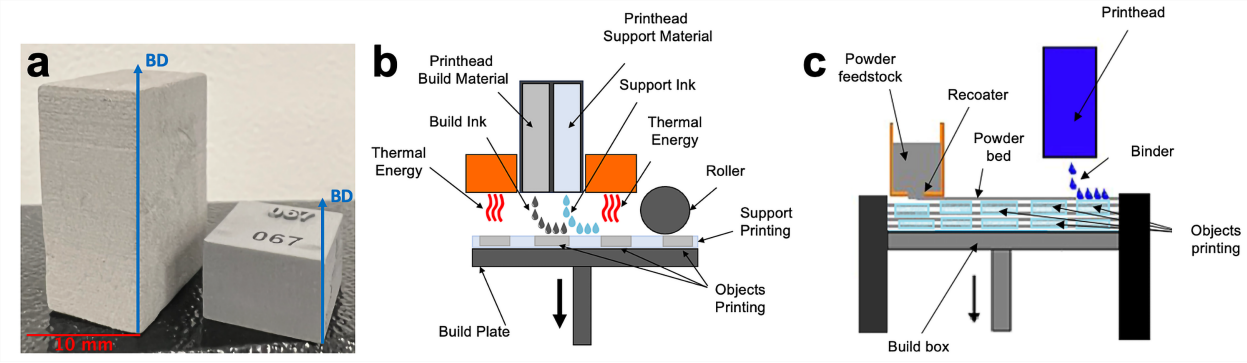

Figure 1. (a) Printed sampled of MMJ (left) and MBJ (right) with build direction indicated by blue arrow. Schematic of (b) MMJ ("Nanoparticle jetting ™") process (c) MBJ processes showing sinter-based AM of SS316L.

For comparison, slightly larger MBJ SS316L samples of 14.99 mm × 20.07 mm × 9.91 mm were fabricated on a Desktop Metal ExOne Innovent 3D Printer system using a proprietary polymeric binder commercialized with the name "CleanFuse" (**Figure 1a**). A schematic of the widely known metal binder jetting process is shown in **Figure 1c**. Gas atomized SS316L powder

from Sandvik Osprey, United Kingdom, of size of D_{90} = 22 μm was used. Powder composition in percent by weight of each element is listed in **Table 1**. The standard processing parameters used for printing are: (i) binder saturation of 85 %, (ii) layer thickness of 100 μm, (iii) drying time of 20 s, (iv) print speed of 150 mm/s, (v) bed temperature of 50 °C. After fabrication, the MBJ build was cured at 180 C for 4hrs in a Yamato DX402C, and subsequently the green samples are manually removed from the powder bed depowdered. At the same manner as for the MMJ process, the green objects are then placed on ceramic plates, and thermally debinded in air atmosphere to the brown state condition. Finally, the brown parts are sintered and densified in a dedicated sintering furnace in hydrogen atmosphere.

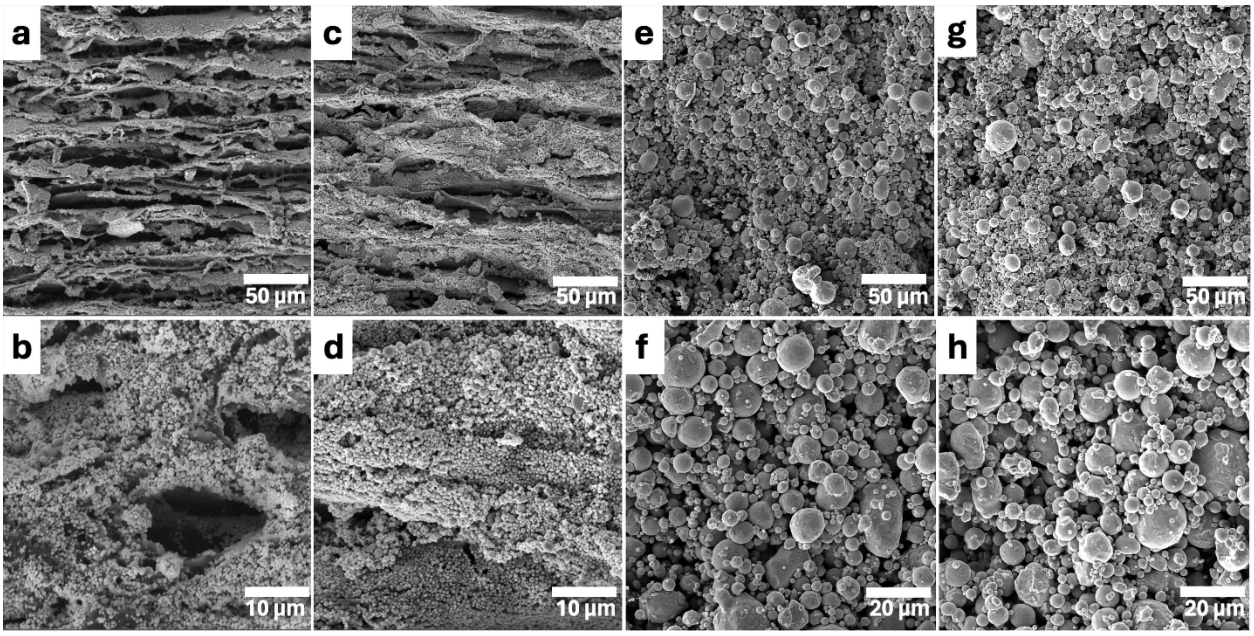

Figure 2. SEM images of samples. (a,b) MMJ green condition. (c,d) MMJ brown condition. (e,f) MBJ green condition. (g,h) MBJ brown condition. Note different magnification of each image.

Figure 2 shows the SEM images of cross sections of the green and brown states of the MMJ and MBJ samples. Specifically, **Figure 2a-2b** show the green state of the MMJ. The carrier-liquid is not present at this stage as it has already evaporated during printing. In the green sample of, the particles are coated with a thin film polymer binder, left after the carrier-liquid evaporates, which

bonds the particles together. The MMJ brown debinded state is also depicted by **Figure 2c-2d**. A clear distinction between the green state and brown state is the visible difference in binder present, which appears to leave more open space between the particles due to the binder component having burned off. It should be noted, however, that there is some residual binder that is left even after debinding that will influence the mechanical properties of the part, however, these effects are still under investigation. **Figure 2e-2f** also shows the green state of the MBJ sample, with the particles bonded together by the polymer binder. **Figure 2g-2h** depicts the brown state in which the binder has been burned off during the debinding stage, although a minimal amount of binder is still present.

2.2 Dilatometry

MMJ and MBJ samples were subjected to dilatometry experiments representative of typical sintering conditions at 1365°C for 4 hours using a heating rate of 5°C per minute in a pure H_2 environment. De-binding of the green part was done at 325°C for 3 hours in a N_2 environment at a heating rate of 4°C/min to obtain the brown part. Note, the MBJ sample were sintered in two stages: first, they were sintered at 900°C for 1 hour in pure H_2 to promote initial neck growth and reduce susceptibility of sample breakage during shipping/handling, and afterwards sintered to final sintering conditions [19]. Note, the amount of shrinkage experienced by the MBJ is expected to be significantly small at the 900 °C (**Figure 10**), and therefore would not influence the basis of its comparison with the MMJ. **Figure 3** gives the time versus temperature profile for dilatometry. Linear shrinkage data for each sample was measured via push-rod dilatometry, with the loading direction parallel to the build direction, which is the direction of the planes of the powder layers, which is indicated by blue axes shown in **Figure 1a**. The densities of the green (e.g., initially printed), brown (de-binded), and full-sintered samples were measured manually by weighing the

samples on a mass balance and measuring the approximate dimensions with Vernier calipers and finding the ratios of the mass to volume. These results are summarized in **Table 2**. The authors also measured the sintered density with the more precise Archimedes principle. It is not possible to use such method for green and brown condition due to the open porosity present in the samples.

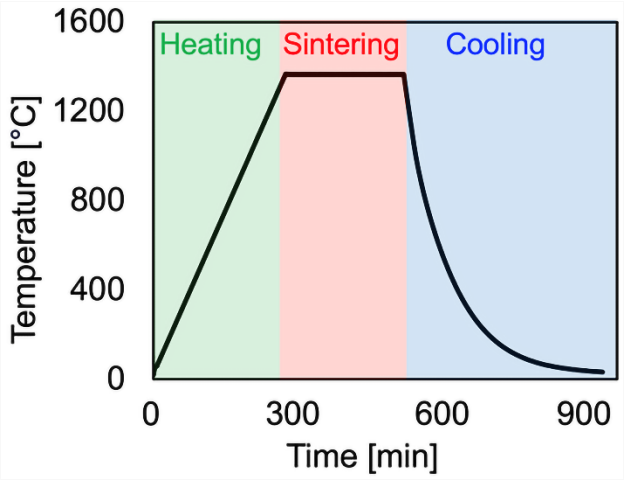

Figure 3. Time versus temperature profile for MMJ and MBJ samples subjected to dilatometry in pure H_2.

Table 1. Chemical Composition of SS316L Powder (Sandvik Osprey, UK) for MBJ, in wt%.

Fe	Cr	Ni	Mo	Mn	Si	C	P	S
Bal.	16-18	10-14	2-3	≤ 2	≤ 1	≤ 0.03	≤ 0.045	≤ 0.03

Table 2. Calculated relative densities of MMJ and MBJ samples

	Green Condition (analytic)	Brown Condition (analytic)	Fully sintered condition (analytic)	Fully sintered condition (archimedes)
MMJ	0.58	0.58	0.97	0.97
MBJ	0.57	0.58	0.96	0.96

2.3 Microstructural characterization

Microstructural characterization was performed on MMJ and MBJ samples subjected to dilatometry. Both samples were cut along the build direction using an abrasive cutter, and hot-mounted on a blend of black Bakelite powder and Conductotherm 3000 using LECO MX 400 mounting press. Each sample surface was ground and polished using 0.05 μm colloidal silica. Thereafter, electron back scatter diffraction (EBSD) was performed using the Tescan Mira 3 FEG scanning electron microscope (SEM) equipped with a EDAX PC for data analysis. X-ray diffraction (XRD) was also done for bulk analysis of sample preferred orientation (texture) and phase information on a Rigaku SmartLab XRD X-ray diffractometer equipped with SmartLab Guidance software for data analysis.

2.4 Mechanical Testing

Displacement-controlled tensile testing on representative samples (e.g., de-binded and sintered under identical conditions) was used to measure the tensile strength and ductility of MMJ SS316L. Twelve (12) total tests were completed using specimens based on the ISO2740 standard. Testing was performed using a servo-electric test stand at a displacement rate of 0.1 mm/min, per the ASTM E8 standard, until failure. Force was recorded during the test using a 25 kN load cell and used to compute engineering stress by dividing by the initial cross-sectional area. Strain was measured using a clip-on extensometer. In conjunction, digital image correlation (DIC) was used

to quantify full-field strain localizations on representative MMJ samples. These samples were prepped for DIC by spray painting the gauge section white and adding a black speckle pattern using an airbrush. The speckle size was small enough to capture the small changes in strain across the length of the coupon. DIC strain data was exported to the VIC 2D software and further assessed using a virtual extensometer spanning the length of the gauge section of the coupon.

2.5 Continuum Sintering Model

To better understand process-property relationships for MMJ versus MBJ SS316L, dilatometry results were used to validate a pressure-less continuum sintering model developed in [19]. The general constitutive relation for a porous medium modeled as a nonlinear-viscous incompressible material with voids is given as:

$$\boldsymbol{\sigma_{ij}} = 2\eta_0 \left[\varphi \dot{\boldsymbol{\varepsilon}}_{\boldsymbol{ij}} + \left(\psi - \frac{1}{3}\varphi\right) \dot{e}\boldsymbol{\delta_{ij}}\right] + P_L \boldsymbol{\delta_{ij}} \quad (1)$$

Where η_0 is the temperature-dependent material shear viscosity of the sample assuming there were no pores, i.e., that of the fully dense material, given by,

$$\eta_0 = A_0 T e^{\left(\frac{Q}{RT}\right)} \quad (2)$$

P_L is the effective sintering stress which depends on surface energy, α, and is given by,

$$P_L = 3\alpha \frac{(1-\theta)^2}{r_0} \quad (3)$$

where r_0 is the radius of the powder particle, or the initial grain size [18]. A_0 is the material-dependent constant shear viscosity pre-exponential and is different for each powder system, T is the absolute temperature and δ_{ij} is the Kronecker delta. φ and ψ are porosity-dependent functions that characterize the normalized shear and bulk moduli of the porous compact respectively. $\dot{e}$ is the first invariant of the strain rate tensor, or the trace of the corresponding matrix, and it corresponds to the volumetric shrinkage rate of the sample. The indexes $i, j = 1, 2, 3$.

In the case of pressure-less sintering, the applied stress $\boldsymbol{\sigma_{ij}} = \mathbf{0}$. Assuming isotropic shrinkage behavior ($\dot{\varepsilon}_x = \dot{\varepsilon}_y = \dot{\varepsilon}_z$) where $x, y,$ and z align with the 1, 2, and 3 indexes for i and j respectively, the strain rate tensor reduces to:

$$\dot{\boldsymbol{\varepsilon}}_{\boldsymbol{ij}} = \begin{bmatrix} \dot{\varepsilon}_z & 0 & 0 \\ 0 & \dot{\varepsilon}_z & 0 \\ 0 & 0 & \dot{\varepsilon}_z \end{bmatrix} \tag{4}$$

Through mass conservation relation, the rate of porosity evolution can also be related to the shrinkage rate as:

$$\frac{\dot{\theta}}{(1-\theta)} = \dot{\varepsilon}_x + \dot{\varepsilon}_y + \dot{\varepsilon}_z = 3\dot{\varepsilon}_z \equiv \dot{e} \tag{5}$$

Where θ denotes the fractional porosity. Substituting the zero-stress tensor and equation (2) into (1), the following first order differential equation is obtained for the rate of change in porosity as:

$$\frac{d\theta}{dt} = -\frac{(1-\theta)P_L}{2\eta_0\psi} \tag{6}$$

For the porosity-dependent normalized bulk viscosity, ψ, the model proposed by Hsueh [20] was used, namely:

$$\psi = \frac{2}{3}\frac{(1-\theta)^A}{\theta^B} \tag{7}$$

Here A and B are model constants that are determined through nonlinear regression analysis using the data obtained from the dilatometry experiments. Combining the foregoing equations and rearranging terms, a final analytical equation for porosity evolution is obtained as

$$\frac{d\theta}{dt} = -\frac{9}{\frac{A_0}{\alpha}Te^{\left(\frac{Q}{RT}\right)}2G} \cdot f(\theta)_\psi \tag{8}$$

Where $f(\theta)_\psi$ is:

$$f(\theta)_{\psi} = \frac{\theta^{B}(1-\theta)^{3}}{(1-\theta)^{A}} \tag{9}$$

Here, Q is the activation energy and R = 8.314 J·mol^{-1}·K^{-1} is the molar gas constant respectively, A_0/α material constants that need to be determined for each powder material. In this work the grain radius, G (a time-dependent quantity over the course of the sintering cycle) was assumed to be equal to r_0. The evolution of the grain size is also given by:

$$\frac{dG}{dt} = -\frac{k_0}{3G^2}\left(\frac{1-\rho_c}{2-\rho_c-\rho}\right)^{\frac{3}{2}} \cdot e^{\left(\frac{-Q_G}{RT}\right)} \tag{10}$$

Where k_0 and Q_G are the grain growth pre-exponential term and activation energy, respectively, ρ is the relative density at a given time given by $\rho = (1-\theta)$, and ρ_c is a critical density, which accounts for the effect of pore pinning at grain boundaries on grain growth. During grain growth, the migration of the grain boundaries accumulates pores during the migration which end up inducing a drag force on the moving boundary to slow down grain growth. In other words, under conditions where pore pinning occurs, the curtailed grain growth would mean the density can only approach this critical value. Note, that the function in the bracket goes to 1 as the full theoretical full density is approached [15,19]. The resulting first-order ordinary differential equation (ODE) for the shrinkage is given by:

$$\dot{\varepsilon}_z = \frac{1}{3}\frac{\dot{\theta}}{(1-\theta)} = \frac{1}{3(1-\theta)}\frac{d\theta}{dt} \tag{11}$$

Inserting the expression for $\frac{d\theta}{dt}$ above, the resulting equation for shrinkage in the build direction can then be obtained as:

$$\dot{\varepsilon}_z = -\frac{3}{2\frac{A_0}{\alpha}Te^{\left(\frac{Q}{RT}\right)}G} \cdot \frac{\theta^{B}(1-\theta)^{2}}{(1-\theta)^{A}} \tag{12}$$

Using the temperature and time data from the dilatometry experiment, equations (10) and (12), which are a coupled first order ODEs, are then solved using MATLAB's 4th order Runge-Kutta algorithm. The optimized value for each parameter is presented in **Table 2**. Note, slight differences in parameter values in the present study versus those in [19] are due to the fact that only one sample each of MMJ and MBJ was tested at a single temperature. As in [19], it is likely that more representative (and accurate) values can be obtained via the optimization procedure if more experiments were conducted. Additionally, it is worth mentioning that the apparent activation energy for sintering densification obtained for MMJ by fitting the continuum model to the experimental data was lower than that of the MBJ, which supports the findings from literature about the activation energy for nanoscale and micron-sized powders [4,16,21–23].

Table 3. Optimized model parameters for MMJ and MBJ samples

	r_0 (μm)	A	B	A_0 / α ($sm^{-1}K^{-1}$)	Q ($KJmol^{-1}$)	k_0 ($\mu m^3/s$)	Q_G ($KJmol^{-1}$)	ρ_c (%)
MMJ	0.75	1.13	0.64	$3.10 \cdot 10^2$	149.2	$1.52 \cdot 10^4$	203.6	94.8
MBJ	20	7.41	0.56	10.27	175.2	$8.93 \cdot 10^5$	156.2	94.8

3. Results

3.1 Shrinkage and densification

The experimental and simulated shrinkage values for the MMJ and MBJ samples are presented in **Figure 4**. Overall, MMJ SS316L shows a maximum shrinkage of 18.5% versus 20.4% for the MBJ sample. Interestingly, the MMJ sample shows more rapid sintering, reaching a plateau in shrinkage behavior near 300 minutes (~1200°C), versus ~500 minutes (~1365°C) for the MBJ sample. These results suggest that MMJ sinters more rapidly than MBJ, which can be expected due to the use of sub-micron powders. This can be observed in the early change in shrinkage values

for MMJ sample prior to 200 minutes (~1,000°C) signifying the beginning of densification. Additional analysis on differences in shrinkage (sintering) rates for MMJ and MBJ will be covered in Section 4.1. Overall, maximum shrinkage values for MMJ SS316L match other studies of MMJ Zirconia (18%) in [10], while shrinkage in the MBJ sample also closely matches other studies on MBJ SS316L sintered above 1300°C including Jamalkhani et al. [24] (21.5%) and Mirzababaei et al. [4] (22.6%).

In comparison, the shrinkage model shows excellent agreement in both trend and magnitude for both MMJ and MBJ SS316L dilatometry data (**Figure 4a-4b**). The model predicts a maximum shrinkage of 18.7% versus 18.5% for the experiment in the MMJ sample, a 1.6% error in shrinkage values (**Figure 4a)**. In comparison, the model also shows less satisfactory agreement with the MBJ experimental data, where a shrinkage of 18.7% is predicted compared to 20.4% observed in experiments (an 8.3% error) (**Figure 4b**). Overall, the close agreement between shrinkage experiments and simulations shows that sintering behaviors in MMJ can be effectively simulated using the isotropic continuum sintering model even though sub-micron powders are employed.

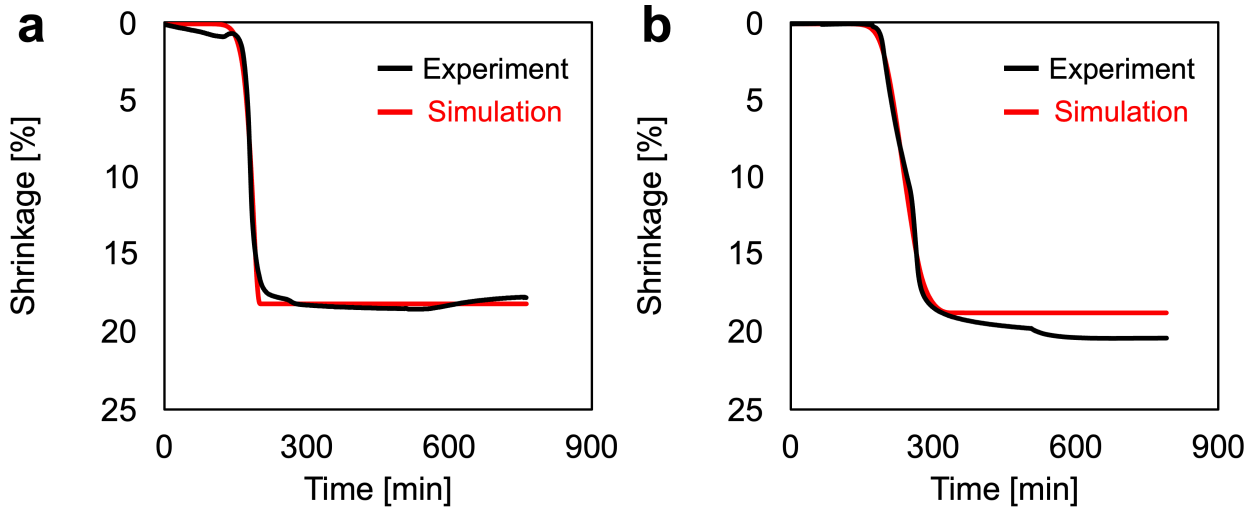

Figure 4. Comparison of 1365°C dilatometry measurements and predicted shrinkage values using isotropic shrinkage model in (a) MMJ and (b) MBJ samples.

279 *3.1 Microstructure*

280 Correlative characterization of the post-sintered MBJ and MMJ samples was performed using
281 EBSD and XRD. **Figure 5** shows a representative image of the grain orientations and morphology
282 within each sample in the form of inverse pole figure (IPF) maps. It is readily apparent that the
283 MMJ microstructure consists of fine, equiaxed grains, with an average grain size <d> of 2.4μm,
284 minimum grain size of d = 0.79μm, maximum grain size of d = 12.0μm (**Figure 5a**). In
285 comparison, the MBJ sample possesses an average grain size <d> of 33.2μm, minimum grain size
286 of d = 16.4μm, maximum grain size of d = 48.0μm (**Figure 5b**). Similar grain size data was
287 reported in [25] in which the authors investigated the shrinkage and densifications behaviors of
288 five samples consisting of different ratios of a mixture of micron and nano-sized 316L powders
289 via powder injection molding. They found that the case of 100% nanoparticles, sintered at 900 °C
290 in H_2, resulted in the smallest average grain size of [43]. An important factor that governs grain
291 growth in sintering is grain boundary migration. However, the high density of grain boundaries
292 associated with the nanoparticles limits this grain boundary migration in a phenomenon known as
293 Zenner pinning, which in turn retards grain growth [25]. Importantly, the grain growth values for
294 MMJ SS316L are an order of magnitude smaller than comparable MBJ SS316L in this study in
295 addition to comparable MBJ Fe-based alloys in the literature such as MBJ SS316L sintered at
296 1380 °C for 120 minutes (<d> = 38 μm) [4] and1385 °C for 180 min (<d> = 86 μm) [25]. Both
297 MMJ and MBJ samples possess a random texture evidenced in the IPF map in **Figure 5a-5b**, in
298 addition to a large fraction of 60° <111> annealing twins are present.

299 **Figure 6a-6b** shows representative images of porosity distribution for MMJ and MBJ samples.
300 As expected, MMJ SS316L has more, but smaller pores compared to the MBJ sample as shown
301 by the cumulative distribution function (CDF) plots in **Figure 6c**. This is due to sintering of sub-

micron powders, as pores not closed from during the grain growth stages will typically remain at grain boundaries (GBs). In comparison, the average pore area in the MMJ samples is 0.47 μm^2 versus 3.43 μm^2 for the MBJ sample. These small values of porosity confirm that the sintering conditions in this study enabled the samples to reach sufficiently high areal densities (**Table 2**). **Figure 7** presents XRD data for both samples; here MMJ shows a single phase, face centered cubic (FCC) structure, while MBJ sample shows both FCC structure and evidence of delta ferrite. Overall, except for fine grain sizes, the MMJ microstructure shows similar morphology and distribution of features as other sinter-based materials densified using solid-state sintering.

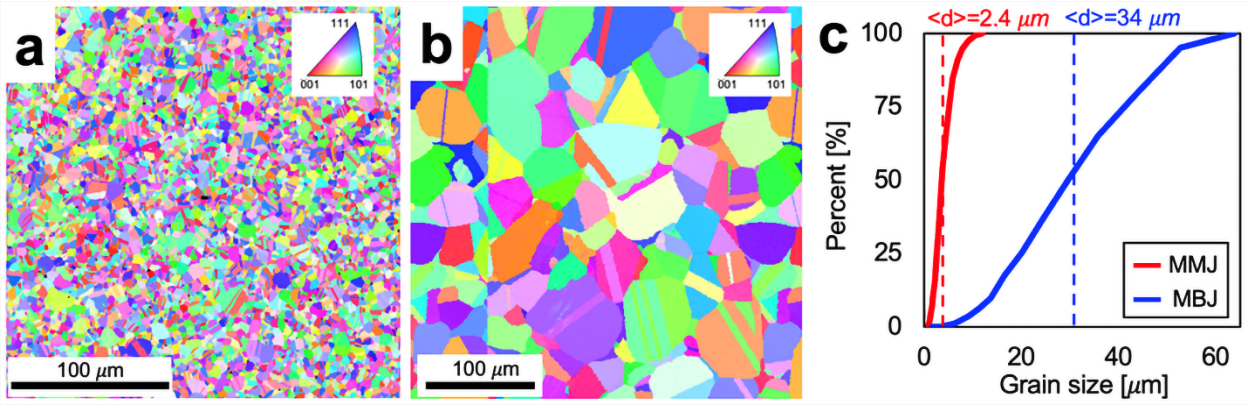

Figure 5. Post sintered microstructure of: (a) MMJ SS316L and (b) MBJ SS316L. (c) CDF of grain size distributions for MMJ (red) versus MBJ (blue).

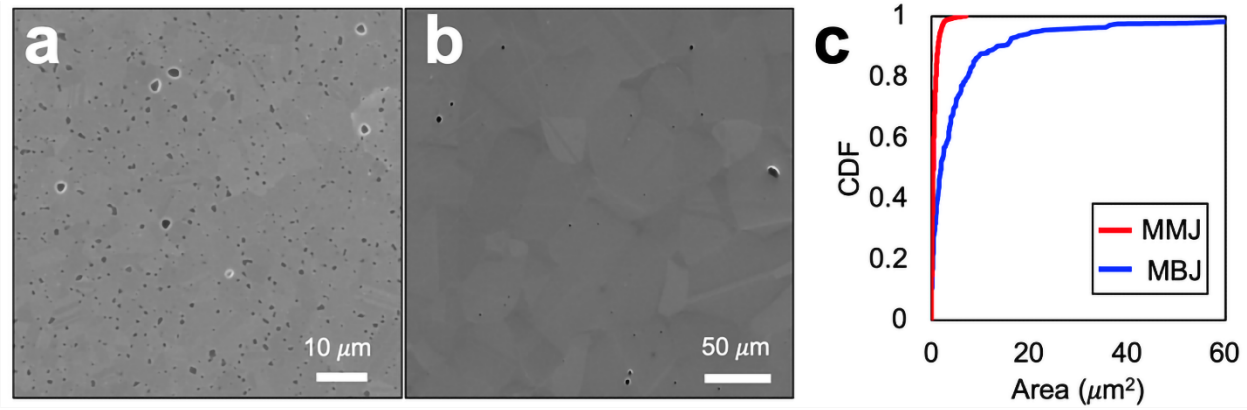

Figure 6. Images of porosity of (a) MMJ and (b) MBJ samples sintered at 1365 °C for 4 hours. (c) Representative empirical CDFs of porosity for MMJ versus MBJ.

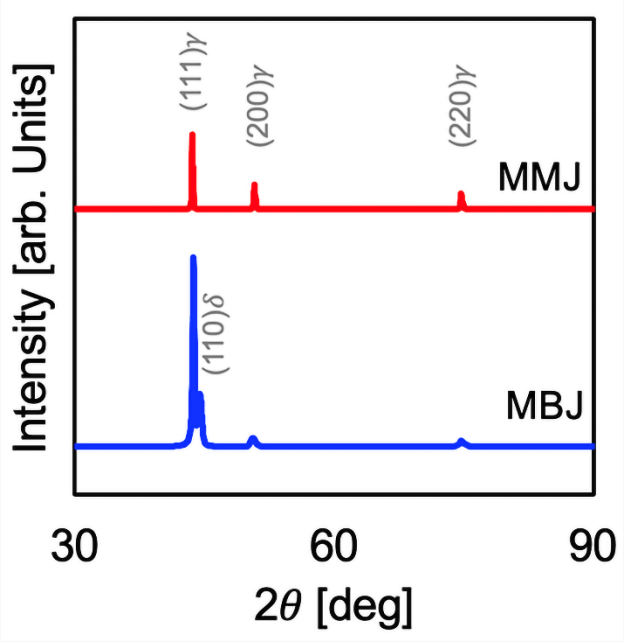

Figure 7. XRD of post-sintered MMJ and MBJ SS316L samples.

3.3 Tensile Behavior

Figure 8 presents box plots for yield strength, ultimate tensile strength, and strain to failure data for the MMJ samples tested under uniaxial tension. It is readily apparent that MMJ samples possess an increased average yield strength (σ_y = 316.9 MPa) and ultimate tensile strength (UTS), σ_{UTS} = 640 MPa, compared to MBJ samples in the literature (yield strength: 191 MPa, 226 MPa, 160 MPa, and 215 MPa and UTS: 544 MPa, 575 MPa, 450 MPa, 535 MPa in references [4,5,6,7]). Remarkably, the high yield strengths and UTS of MMJ samples are on the lower bound for laser-processed SS316L, such as directed energy deposition (DED) [28–30], where strengthening mechanisms are largely governed by sub-grain cellular structures and high dislocation densities that occur under rapid solidification processing [28,31]. However, MMJ samples show a significant reduction in average strain to failure (ε_f = 15.5%) compared to what has been reported on MBJ SS316L (~40-90%) in the literature [28,31]. This is shown by the DIC images in **Figure 9**, denoting a flat fracture surface indicative of brittle fracture under tensile loading. These results

suggests that unique microstructures created using MMJ suffer from the traditional strength-ductility tradeoff.

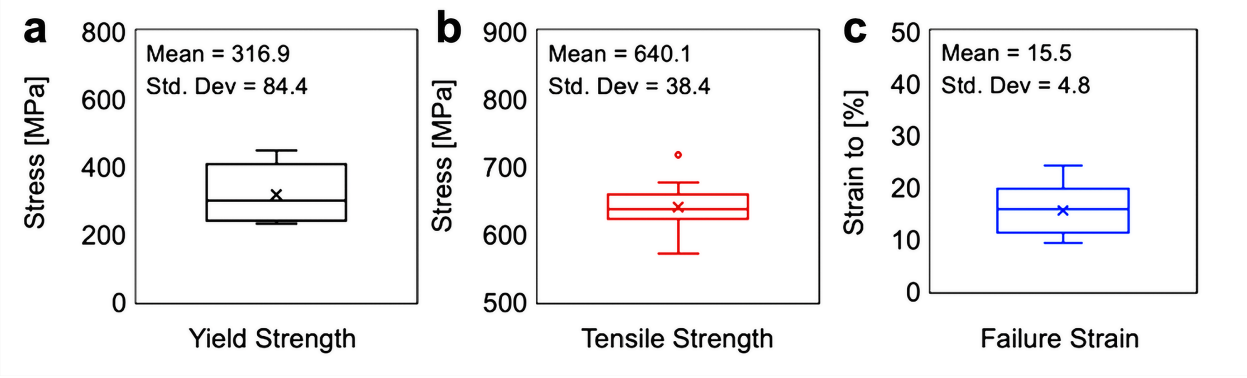

Figure 8. Box plots showing mean and standard deviation of: (a) Yield stress, (b) ultimate tensile strength, and (c) strain to failure for MMJ tensile samples for twelve samples.

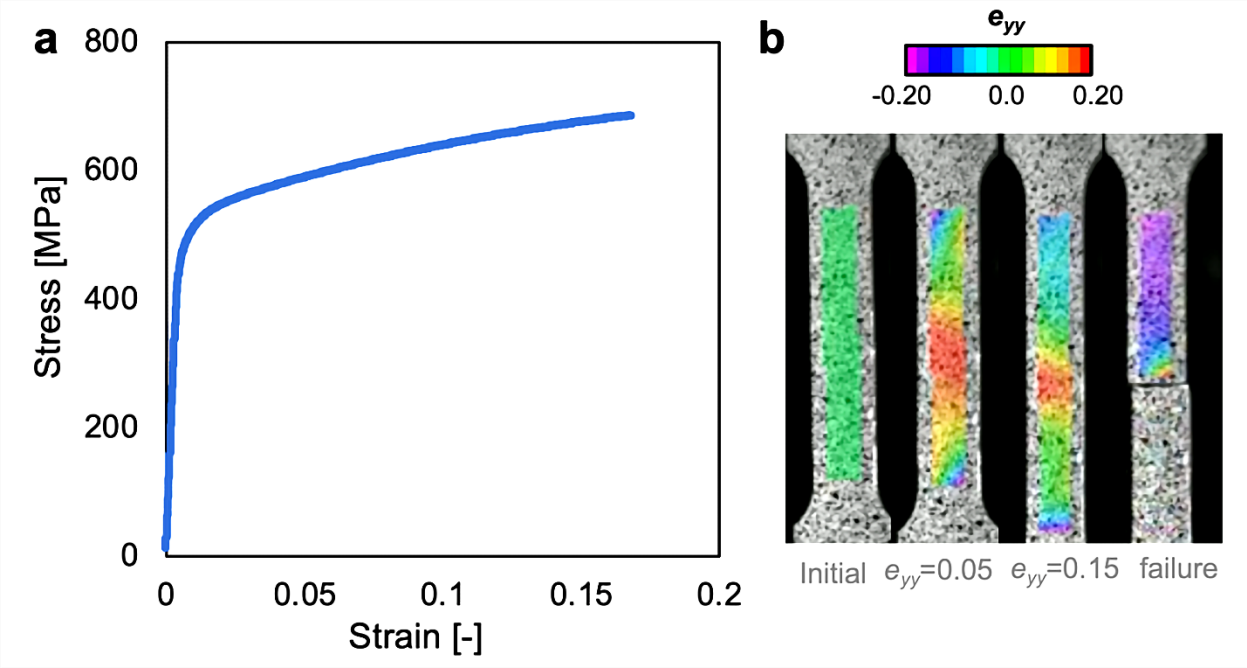

Figure 9. (a) Representative engineering stress-strain curve of MMJ SS316L under uniaxial tension loading. (b) DIC images showing strain localization within the gauge region.

4. Discussion

4.1 Densification of micron and nano sized powders

Densification is the process of pore elimination during solid-state sintering to achieve a density close to theoretically fully density, as the material density without any pores. The main mechanism of densification is pore elimination which is the result of a combination of different mass transport mechanisms such as lattice and grain boundary diffusion. The most widely used model for solid state sintering is that of Coble [48], in which the author classified sintering as a three-stage process; initial, intermediate, and final. The bulk of densification is believed to occur during the intermediate stage.

For micron-sized powders, the initial stage of sintering begins with contact formation and neck growth. As temperature increases and depending on whether there is external pressure being applied, powder particles form contacts. As the temperature is further increased these contact points begin to grow due to mass being deposited at this junction from the particle surface through surface diffusion. It must be noted that surface diffusion does not contribute to the eventual densification. In MBJ of SS316L, this is manifest in the initial strength that is gained after binder burn off to obtain the brown sample, which is strong enough to withstand handling stresses. The intermediate and final stages are characterized by pore channeling and pore isolation and rounding respectively. Densification is achieved as the particle center-to-center distance shrinks due to mass diffusion across grain boundary via grain boundary and lattice diffusion.

For nanoparticles, however, most of the concepts from Coble's development do not apply directly. At the nanometric scale, most of the arguments from the two-spherical particles perspective may cease to hold. Particle size varies rapidly during nanosintering, and factors like agglomeration and green density nonuniformity make it challenging to sustain microstructural evolutions. Due to its linear equation origins, the standard scaling law may not apply to nanosintering. Nonlinear diffusion behavior of nanosintering and size-dependent diffusion

activation energies affect the diffusion flow expressions [54]. Hence, most of the literature on solid-state sintering of nanoparticles are qualitative results from experimental observations [23,49]. For example, J.W. Oh et. al found that sintering of Fe nanoparticles resulted in a double peak response on a shrinkage rate versus temperature plot which they attributed to nanoparticle agglomeration. Thus, the densification of nanoparticles is two-fold, first, the elimination of intra-agglomerated pores followed by those of inter-agglomerates. The former involves the removal of pores within individual agglomerates or clusters whereas the latter deals with the removal of pores between several contacting agglomerates of nanoparticles. It is the authors' belief that the observed dip in the shrinkage of MMJ in **Figure 10** is a manifestation of the double peaks observed in [23,49], although further analysis is warranted.

4.2 Sintering rate and driving force for densification

It is readily observable that the unique microstructure and mechanical behavior of MMJ SS316L is linked to a distinctive sintering response. In particular, significant dissimilarities in the MMJ sintering response can be observed in the early stages of sintering. This can be seen in **Figure 10a**, which compares the experimental shrinkage versus the temperature for MMJ and MBJ. Interestingly, the MMJ sample undergoes significant shrinkage between 850 and 1,000°C, reaching a value of 15% at 1,000°C (or ~81% of the maximum expected shrinkage) compared to 1.5% shrinkage for MBJ sample at 1,000°C. This behavior can be expected, as sub-micron powders possess a substantially increased surface area (and thus surface energy), which is a key driving force for sintering [32]. Also, sub-micron powders typically possess lower sintering activation energy, the minimum energy required to initiate the sintering process [23]. This is a one factor in why nanoscale powders possess reduced sintering temperatures and increased driving forces for densification compared to micron-sized powders [12].

To better understand the mechanisms behind enhanced MMJ shrinkage rates, the continuum sintering model was employed. In this model, the overall shrinkage is linearly related to the effective sintering stress, defined the change in free surface energy with respect to the volumetric shrinkage, and inversely related to the shear viscosity, and normalized bulk modulus which is a function of porosity. Importantly, this sintering stress is linearly correlated to the specific surface energy, the square of the initial density, and the inverse of the average powder particle radius. Therefore, the use of sub-micron powders in MMJ can be expected to result in a substantial increase in sintering stress, which is the driving force for densification [33,34]. The MMJ's sintering stress also benefit from the early densification, thanks to the sub-micron sizes and lower activation energy. The quadratic dependence of the sintering stress on the relative density implies that the higher earlier densifications also complement the large overall sintering stress observable in the MMJ samples. For large powders, the sintering stress is too small to overcome inherent compact strength that resists densification [27,33,35]; however, the reduction of powders from micron to sub-micron sizes can lead to an order of magnitude increase in the sintering stress [36]. This is shown in **Figure 10b,** which compares the sintering rate e.g., the sintering stress normalized by the shear viscosity o P_L/η_0 (units of $1/s$) for MMJ and MBJ samples. It can be readily observed that the sintering rate for MMJ sample is approximately 3-times greater than the MBJ sample (**Figure 10b**). Therefore, this is the most likely explanation as to why the MMJ observed enhanced shrinkage rates compared to the MBJ samples. Overall, the model confirms that the substantial enhancement in shrinkage rate in the MMJ samples is due to sub-micron powder sizes. These results also suggest that MMJ samples could be sintered to full (or near full) density at significantly lower temperatures, therefore reducing the potential for part distortion of complex shapes or the formation of undesirable delta ferrite (δ) which is stable in austenitic stainless steels in the

temperature range 1205–1438°C [37] (**Figure 7b**). Additional insight into the differences between the sintering behaviors of sub-micron powders compared to traditional micron-scale powders are warranted, such as the potential reduction of activation energy or promotion of super-solidus sintering due to reduced melting temperatures [12,25].

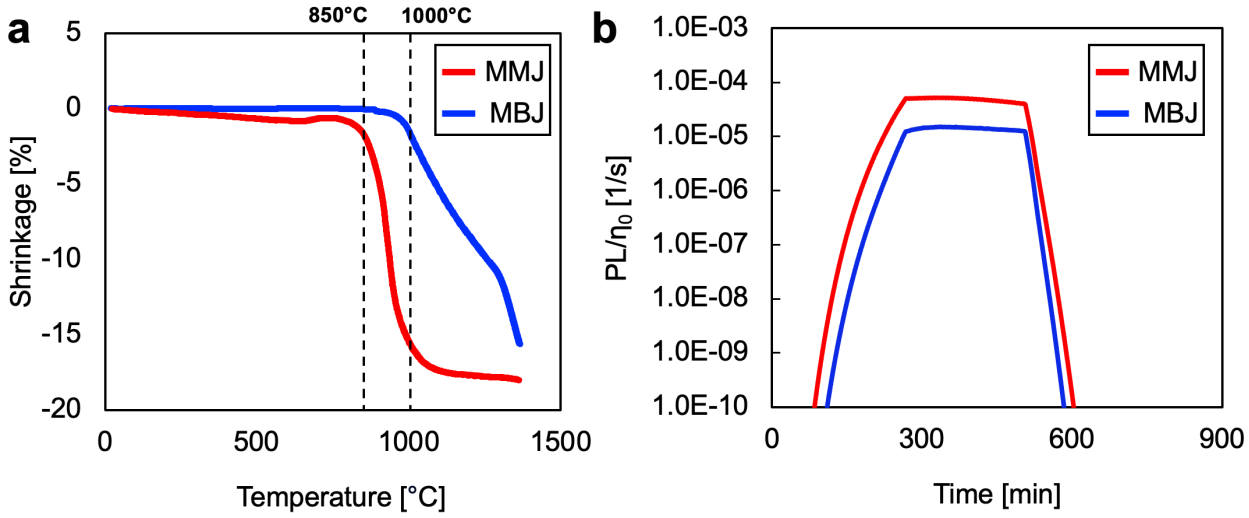

Figure 10. (a) Shrinkage versus temperature (b) simulated sintering rate versus time ~~and~~ for MMJ and MBJ samples.

4.3 Simulated porosity evolution and grain growth

As covered above, MMJ SS316L possesses unique process-microstructure relationships due to the use of sub-micron powders. It is well-known that microstructure is intimately linked with mechanical properties, in particular defect distributions and grain size/morphology [38–40]. To better assess the relationships between shrinkage behaviors and microstructure formation in MMJ, the continuum sintering model was used to evaluate the evolution of porosity and grain size. **Figure 11a** presents the change in porosity with time for the MMJ and MBJ samples. Interestingly, these curves follow the same trends and possess similar magnitudes. In more detail, the MMJ sample starts with slightly lower but albeit negligible porosity compared to the MBJ sample (42% versus 43%, respectively). The model predicts a final porosity value of 3.5% and 4.6% for MMJ and MBJ samples which are very close with the final experimental density values in **Table 2**

(~97% and ~96% for MMJ and MBJ respectively). Overall, the model for MMJ SS316L reproduces well-known trends in sinter-based AM that smaller values of initial porosity result in higher densities after sintering. However, the evolution of porosity does not capture the enhanced shrinkage (sintering) rate of MMJ SS316L observed experimentally as shown by the similar porosity evolution curves.

In comparison, simulated grain growth behaviors in **Figure 11b** show significant deviation between MMJ and MBJ SS316L. Considerably less grain growth is observed for MMJ samples (~30% increase in average grain size) versus ~60% increase in average grain size for MBJ. Interestingly, the model predicts that grain growth in MMJ begins at ~230 minutes (1150 °C) which can be seen from the grain growth-temperature vs time plot in **Figure 11b**, which agrees with experimental shrinkage curves in **Figure 10** that shows minimal shrinkage beyond this temperature signifying that grain growth as opposed to densification is occurring. However, the model predicts grain growth for the MBJ sample begins at 280 minutes (1365 °C) at which point densification has commenced. This is in line with the findings of [38–40] for SS316L fabricated via powder metallurgy and MBJ. Grain growth for both samples commence at approximately 502 minutes (1365°C), resulting in an approximate (linear) grain growth rate of 1.025E-10^{-10} $m \cdot s^{-1}$ and 1.05E-10^{-9} $m \cdot s^{-1}$ for MMJ and MBJ, respectively. A potential reason for the enhanced grain growth rate of MBJ compared to MMJ may be Zener pinning mechanism, however additional analyses are warranted.

However, care must be taken when directly comparing simulated MMJ to MBJ behaviors for microstructure development, as internal powder compact behaviors are intimately linked to sintering mechanisms that may be differ between sub-micron versus micron-scale particles. For example, as mentioned in Section 4, although nanoscale powders are known to possess reduced

activation energies, the fitting resulted in a larger grain growth activation energy (Q_G) that was used in this study for MMJ samples. It is deduced that the incorporation of lower apparent and grain growth activation energies could potentially capture the difference in shrinkage effects seen before 850 °C in MMJ (**Figure 10a**). Notwithstanding, determinations of activation energy are at best estimates, as they depend on a wide range of factors such as material, temperature, diffusion mechanism, geometry, rate of heating, etc. As such a combination of experimental, numerical, and sometimes analytical approaches is used to obtain estimates, and that is beyond the scope of this study. Overall, further investigations are necessary to identify the specific sintering mechanisms for sub-micron MMJ powders. For example, novel techniques surrounding the use of *in situ* electron and x-ray microscopy [41,42] show great promise in directly mapping sintering mechanisms through direct measurement of powder properties (i.e., neck growth, dihedral angles, etc.) during sintering. These properties can then be used to identify which mechanisms are dominant via standard sintering relationships [43,44]. Overall, such these analyses could provide important insight on local powder compact behaviors and provide important data for simulation parameter identification and should be considered as future studies.

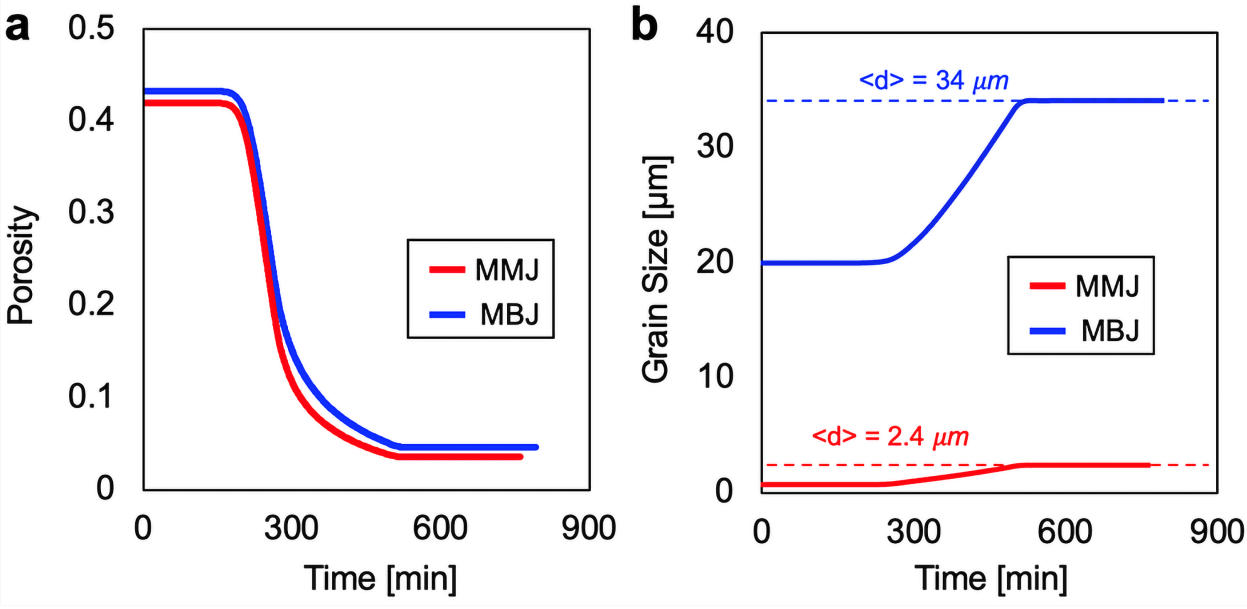

Figure 11. Simulated (a) fractional porosity and (b) grain growth versus time for MMJ versus MBJ samples.

4.4 Strengthening mechanisms and effect of porosity on tensile behavior

The increased yield strength in MMJ is largely due to grain size strengthening and can be elucidated using the typical Hall-Petch relation, where a decrease in grain size is accompanied by the increase of grain boundaries that present obstacles preventing dislocation motion [45]. However, materials densified using solid state sintering generally suffer from high levels of incident porosity that significantly reduce yield stress; indeed, this is one of the key explanations as to why MBJ materials suffer from reduced flow stresses compared to wrought and other AM technologies [2]. To assess the competing role of grain size (d) strengthening and porosity volume fraction (f) on the yield strength (σ_Y) in MMJ, an empirical relation based on Hall-Petch equation recently employed with good success for MBJ SS316L was used, namely: $\sigma_Y = \sigma_{Y,0} \cdot exp(-6.5f)$ [4,14]. Here, the initial yield stress $\sigma_{Y,0} = \sigma_0 + Kd^{-\frac{1}{2}}$ is obtained using the well-known Hall-Petch relation (where σ_0 = 188 MPa and K = 275 MPaμ·$m^{\frac{1}{2}}$ are constants at given strain used in [4] and d is the average grain size). Using an average grain size of 2.4 μm and pore volume fraction f = 3.183% determined from post-mortem SEM images, a value of σ_Y = 296 MPa is obtained for the MMJ SS316L material. This is in good agreement with the experimentally measured value of σ_Y= 316.9 MPa (e.g., resulting in only an 6.5% difference between experiment and analytical predictions). These results clearly show that grain boundary strengthening is the dominant mechanism for increased flow stress in MMJ. Furthermore, with other sinter-based technologies, maximal strength gains are reduced by incident porosity. Thus, even though recently sinter-based AM applications have been used to manufacture critical components, additional enhancements in

processing and sintering conditions that further minimize porosity and increase flow stress need to be explored for the MMJ components.

Comparatively, the reduced strain to failure values of MMJ can also be understood as a function of the distribution of fine grain sizes within the microstructure. Flipon et al. [46] quantified an increase in yield strength and reduction in failure strain for SS316L made by spark plasma sintering (SPS). That study showed that the reduction of grain size from 15µm to 0.3 µm led to considerably reduced plastic strain to failure (from 45% for $<d>$ = 15µm to 0.15% for $<d>$= 0.3µm). While the behavior in yield strength versus grain size was captured by a linear trend, plastic strains to failure for grain sizes between 1.4 – 3µm ranged from 13% to 40%, indicating substantial variability. Although the authors in this study mentioned that variability in plastic failure strain depends on the grain size distribution, they did not provide a potential mechanism for such behaviors. Interestingly, for MMJ SS316L in this study, the average grain size $<d>$ = 2.4µm falls between this range of large failure strain variability discovered in Flipon. This is also evidenced by average failure strains of 15.5%, which is within the 13% to 40% range of Flipon et al. [46]. CDF plots of grain size in **Figure 5c** show that 50% of grains are smaller than the mean of $<d>$ = 2.4µm. Additionally, CDF plots show heavy lower tail behaviors, evidence of large numbers of fine grains within the microstructure.

From the tensile results above, it can clearly be seen that there is a strength-ductility tradeoff for the MMJ sample. This behavior of larger strength vs lower ductility is typical of AM 316L, usually due to the inherent porosity in the sintered parts. The enhancement in ductility that is can sometimes accompany the Hall-Petch strengthening from grain refinement seems to be, at best, minimal in this case. The authors believe the discrepancy stems from the fact that reducing grain size can also help in suppressing local stress concentration resulting from dislocation pile-up and

thereby improving ductility. However, in general for single phase materials, reduction in grain size does not imply an increase in both strength and ductility. Hall-Petch relation does not predict increase in ductility with decreasing grain size. In most cases, increase in strength results in a decrease in ductility, which is evident in the case of this MMJ. The lack of apparent ductility from the tensile tests could be attributed to several factors. One possibility is that in fine grained microstructure there is an increased chance of grain boundary sliding, rather than dislocation, that governing the deformation. This curbs the material's ability to deform plastically while adopting a more fracture-type deformation behavior [51]. Another possibility is that, in finer grains, even though yield strength might be enhanced, there is a possibility of elemental (e.g., N, S, O, etc) impurities being trapped at the grain boundaries which could favorably act as cites for crack initiation, leading to the observed post-yield brittle behavior observed in the MMJ [52,53].

Although qualitative, the statistical distributions of fine grain sizes in MMJ SS316L indicate the plausibility that large numbers of fine grains do indeed strongly influence the failure strain properties. While more analysis is necessary, the heavy lower tail behaviors and large numbers of fine grains below 3μm (e.g., the transition region for failure strain in [46]) are the likely source of ductility loss compared to other sinter-based AM processes in the literature [46,47]. These results also suggest that yield, ultimate tensile strength, and failure strain of MMJ materials can be further controlled by tuning the overall sintering process and post-treatment annealing to regulate grain growth. As such, additional studies on heat treatment in MMJ, although out of the scope of the present paper, are warranted.

5. Conclusions

This study leveraged novel "drop on demand" Metal Material Jetting (MMJ) of sub-micron powders to fabricate SS316L samples subjected to dilatometry, mechanical testing, and correlative

materials characterization. These data were compared to Metal Binder Jet (MBJ) SS316L to evaluate differences in process-structure-property relationships between the two processes. Overall, the following conclusions can be drawn from this study:

- Densification behaviors for SS316L processed by MMJ are largely similar to MBJ under the identical sintering conditions (1365 °C for 4 hours in pure H_2). Overall, part shrinkage (18.5%) and final density (97%) in MMJ SS316L are comparable to MBJ SS316L (20.4% shrinkage and 96% density).
- Average grain sizes in fully sintered MMJ SS316L (2.4μm) are more than an order of magnitude smaller than MBJ SS316L (34μm). This results in an average yield strength of 312 ± 84 MPa and ultimate tensile strength 640 ± 38, drastically exceeding values for MBJ S316L in the literature. However, the fine grain sizes also resulted in significantly lower average failure strains to mean value of 15.5 ± 4.8%. This was attributed to the large number of fine grains within the microstructure, which are known to lead to high strength but low ductility.
- An isotropic pressure-less sintering model agreed well with experimental shrinkage data for both MMJ and MBJ SS316L. This indicates that continuum sintering models, typically employed for micron-scale powders, can also be leveraged for sub-micron powders even though they may densify by different mechanisms. However, simulated behaviors for the evolution of internal powder compact properties (i.e., porosity and grain sizes) showed some discrepancies with shrinkage results and sintering theory. This was attributed to a lack of accurate knowledge of simulation parameters and sintering mechanisms in sub-micron SS316L powders.

- Sintering rates for MMJ SS316L are significantly increased compared to MBJ SS316L. Overall, non-negligible powder compact shrinkage began at ~850 °C, and reached 81% of the final shrinkage values by 1000 °C. The reason behind this behavior was characterized as typical mechanisms observed in nanoscale powders, namely: (i) the decrease in sintering temperature and (ii) a three-fold increase in sintering stress compared to MBJ determined via the isotropic pressure-less sintering model.

Overall, this study provides important insight into the process-property relationships for sinter-based AM materials using sub-micron powders, which show promise in overcoming traditional strength limitations in MBJ and metal injection molding (MIM) technologies that rely on micron-sized powders. As such, additional experimental insight on process-structure-property relationships for MMJ (and related sub-micron technologies) are needed, such as further understanding on the sintering mechanisms and kinetics to prescribe optimized annealing thermal treatments for MMJ materials.

Acknowledgements

The authors would like to thank Eric Poczatek, Joy Forsmark, and Yun Bai at Ford Motor Company for assistance with sample de-binding and Bryan Sherman at DSH Technologies for assistance with sample dilatometry. The authors would also like to thank Amit Misra for helpful discussions. This work was supported by NSF DMR- 2237433. The authors acknowledge the financial support of the University of Michigan College of Engineering and NSF grant #DMR-0320740, and technical support from the Michigan Center for Materials Characterization.

References

[1] A. Mostafaei, A.M. Elliott, J.E. Barnes, F. Li, W. Tan, C.L. Cramer, P. Nandwana, M. Chmielus, Binder jet 3D printing—Process parameters, materials, properties, modeling, and challenges, Prog Mater Sci 119 (2021). https://doi.org/10.1016/j.pmatsci.2020.100707.

[2] N. Huang, O.J. Cook, A.P. Argüelles, A.M. Beese, Review of Process–Structure–Property Relationships in Metals Fabricated Using Binder Jet Additive Manufacturing, Metallography, Microstructure, and Analysis (2023). https://doi.org/10.1007/s13632-023-00998-4.

[3] A. Mostafaei, C. Zhao, Y. He, S. Reza Ghiaasiaan, B. Shi, S. Shao, N. Shamsaei, Z. Wu, N. Kouraytem, T. Sun, J. Pauza, J. V. Gordon, B. Webler, N.D. Parab, M. Asherloo, Q. Guo, L. Chen, A.D. Rollett, Defects and anomalies in powder bed fusion metal additive manufacturing, Curr Opin Solid State Mater Sci 26 (2022). https://doi.org/10.1016/j.cossms.2021.100974.

[4] S. Mirzababaei, B.K. Paul, S. Pasebani, Microstructure-property relationship in binder jet produced and vacuum sintered 316 L, Addit Manuf 53 (2022). https://doi.org/10.1016/j.addma.2022.102720.

[5] P. Kumar, J. Radhakrishnan, S.S. Gan, A. Bryl, J. McKinnell, U. Ramamurty, Tensile and fatigue properties of the binder jet printed and hot isostatically pressed 316L austenitic stainless steel, Materials Science and Engineering: A 868 (2023). https://doi.org/10.1016/j.msea.2023.144766.

[6] T. Tancogne-Dejean, C.C. Roth, D. Mohr, Rate-dependent strength and ductility of binder jetting 3D-printed stainless steel 316L: Experiments and modeling, Int J Mech Sci 207 (2021). https://doi.org/10.1016/j.ijmecsci.2021.106647.

[7] J. Cai, B. Zhang, X. Qu, Microstructure evolution and mechanical behavior of SS316L alloy fabricated by a non-toxic and low residue binder jetting process, Appl Surf Sci 616 (2023). https://doi.org/10.1016/j.apsusc.2023.156589.

[8] Y. Bai, C.B. Williams, The effect of inkjetted nanoparticles on metal part properties in binder jetting additive manufacturing, Nanotechnology 29 (2018). https://doi.org/10.1088/1361-6528/aad0bb.

[9] C.W. Gal, D.S. Shin, C. Lee, S.J. Park, D.Y. Park, Rheological Behavior of Water-Atomized 316L Stainless Steel Powder Depending on Particle Size, Metals and Materials International (2023). https://doi.org/10.1007/s12540-023-01441-7.

[10] Y. Oh, V. Bharambe, B. Mummareddy, J. Martin, J. McKnight, M.A. Abraham, J.M. Walker, K. Rogers, B. Conner, P. Cortes, E. MacDonald, J.J. Adams, Microwave dielectric properties of zirconia fabricated using NanoParticle Jetting™, Addit Manuf 27 (2019) 586–594. https://doi.org/10.1016/j.addma.2019.04.005.

[11] S. Zhong, Q. Shi, Y. Deng, Y. Sun, C. Politis, S. Yang, High-performance zirconia ceramic additively manufactured via NanoParticle Jetting, Ceram Int 48 (2022) 33485–33498. https://doi.org/10.1016/j.ceramint.2022.07.294.

[12] O. Dominguez, Y. Champion, J. Bigot, Liquidlike Sintering Behavior of Nanometric Fe and Cu Powders: Experimental Approach, Metallurgical and Materials Transactions A 29 (1998) 2941–2949. https://doi.org/https://doi.org/10.1007/s11661-998-0201-3.

[13] C. Kenel, N.P.M. Casati, D.C. Dunand, 3D ink-extrusion additive manufacturing of CoCrFeNi high-entropy alloy micro-lattices, Nat Commun 10 (2019). https://doi.org/10.1038/s41467-019-08763-4.

[14] S.L. Taylor, A.E. Jakus, R.N. Shah, D.C. Dunand, Iron and Nickel Cellular Structures by Sintering of 3D-Printed Oxide or Metallic Particle Inks, Adv Eng Mater 19 (2017). https://doi.org/10.1002/adem.201600365.

[15] R.M. German, Coarsening in sintering: Grain shape distribution, grain size distribution, and grain growth kinetics in solid-pore systems, Critical Reviews in Solid State and Materials Sciences 35 (2010) 263–305. https://doi.org/10.1080/10408436.2010.525197.
[16] S.K. Manchili, J. Wendel, E. Hryha, L. Nyborg, Sintering of bimodal micrometre/nanometre iron powder compacts - A master sintering curve approach, Powder Technol 391 (2021) 557–568. https://doi.org/10.1016/j.powtec.2021.06.052.
[17] G. Lynnora O, A. Magdi B, C. Reid J, H.I. Fred C, C. Zachary C, Mitigating Distortion during Sintering of Binder Jet Printed Ceramics, Conference: Solid Freeform Fabrication Symposium 2018 (2018) 135–142. https://repositories.lib.utexas.edu/bitstream/handle/2152/90083/2018-10-Grant.pdf?sequence=2&isAllowed=y.
[18] C.C. M. Forgiarini, Metal Binder Jetting and Metal Material Jetting as complementary technologies: a user perspective, Advances in Additive Manufacturing with Powder Metallurgy, , in: Proceedings of AMPM2023 Conference, 2023.
[19] A. Cabo Rios, E. Olevsky, E. Hryha, M. Persson, R.K. Bordia, Analytical models for initial and intermediate stages of sintering of additively manufactured stainless steel, Acta Mater 249 (2023). https://doi.org/10.1016/j.actamat.2023.118822.
[20] C.H. Hsueh, A.G. Evans, R.M. Cannon, R.J. Brook, Viscoelastic stresses and sintering damage in heterogeneous powder compacts, Acta Metall 34 (1986) 927–936.
[21] B.E. Kashyap, K. Tangri, Grain growth behaviour of type 316L stainless steel, Materials Science and Engineering: A 149 (1992) 13–16.
[22] Z.Y. Liu, N.H. Loh, K.A. Khor, S.B. Tor, SINTERING ACTIVATION ENERGY OF POWDER INJECTION MOLDED 316L STAINLESS STEEL, 2001. www.elsevier.com/locate/scriptamat.
[23] J.W. Oh, Y. Seong, D.S. Shin, S.J. Park, Investigation and two-stage modeling of sintering behavior of nano/micro-bimodal powders, Powder Technol 352 (2019) 42–52. https://doi.org/10.1016/j.powtec.2019.04.056.
[24] M. Jamalkhani, M. Asherloo, O. Gurlekce, I.T. Ho, M. Heim, D. Nelson, A. Mostafaei, Deciphering microstructure-defect-property relationships of vacuum-sintered binder jetted fine 316 L austenitic stainless steel powder, Addit Manuf 59 (2022). https://doi.org/10.1016/j.addma.2022.103133.
[25] R.M. German, Supersolidus Liquid-Phase Sintering of Prealloyed Powders, Metallurgical and Materials Transactions A 28 (1997) 1553–1567.
[26] R. Batmaz, A. Zardoshtian, T.D. Sabiston, R. Tangestani, A. Chakraborty, N. Krutz, S. Pendurti, A. Natarajan, E. Martin, An Investigation into Sinterability Improvements of 316L Binder Jet Printed Parts, Metall Mater Trans A Phys Metall Mater Sci 53 (2022) 915–926. https://doi.org/10.1007/s11661-021-06564-3.
[27] D.Y. Park, S.W. Lee, S.J. Park, Y.S. Kwon, I. Otsuka, Effects of particle sizes on sintering behavior of 316L stainless steel powder, Metall Mater Trans A Phys Metall Mater Sci 44 (2013) 1508–1518. https://doi.org/10.1007/s11661-012-1477-x.

[28] T.R. Smith, J.D. Sugar, C. San Marchi, J.M. Schoenung, Strengthening mechanisms in directed energy deposited austenitic stainless steel, Acta Mater 164 (2019) 728–740. https://doi.org/10.1016/j.actamat.2018.11.021.
[29] L. Simoneau, A. Bois-Brochu, C. Blais, Tensile Properties of Built and Rebuilt/Repaired Specimens of 316L Stainless Steel Using Directed Energy Deposition, J Mater Eng Perform 29 (2020) 6139–6146. https://doi.org/10.1007/s11665-020-05087-z.
[30] D.R. Feenstra, V. Cruz, X. Gao, A. Molotnikov, N. Birbilis, Effect of build height on the properties of large format stainless steel 316L fabricated via directed energy deposition, Addit Manuf 34 (2020). https://doi.org/10.1016/j.addma.2020.101205.
[31] K.M. Bertsch, G. Meric de Bellefon, B. Kuehl, D.J. Thoma, Origin of dislocation structures in an additively manufactured austenitic stainless steel 316L, Acta Mater 199 (2020) 19–33. https://doi.org/10.1016/j.actamat.2020.07.063.
[32] S.-J.L. Kang, Sintering, Densification, Grain Growth, & Microstructure, (n.d.).
[33] R.M. German, Manipulation of Strength During Sintering as a Basis for Obtaining Rapid Densification without Distortion, Mater Trans 42 (2001) 1400–1410. https://doi.org/10.2320/matertrans.42.1400.
[34] L.O. Grant, M.B. Alameen, J.R. Carazzone, C. Fred, H. Iii, Z.C. Cordero, Mitigating Distortion During Sintering of Binder Jet Printed Ceramics, in: Solid Freeform Fabrication Symposium , 2018.
[35] S. Sadeghi Borujeni, A. Shad, K. Abburi Venkata, N. Günther, V. Ploshikhin, Numerical simulation of shrinkage and deformation during sintering in metal binder jetting with experimental validation, Mater Des 216 (2022). https://doi.org/10.1016/j.matdes.2022.110490.
[36] Z. Chen, F. Li, W. Chen, D. Zhu, Z. Fu, Numerical Simulation of Particle Size Influence on the Sintering Behavior of 316L Stainless Steel Powders Fabricated by Binder Jet 3D Printing, J Mater Eng Perform 30 (2021) 3705–3717. https://doi.org/10.1007/s11665-021-05709-0.
[37] B. Arh, F. Tehovnik, F. Vode, Transformation of the δ-ferrite in ss2343 austenitic stainless steel upon annealing at 1050◦c, 1150◦c and 1250◦c, Metals (Basel) 11 (2021). https://doi.org/10.3390/met11060935.
[38] A. Vagnon, O. Lame, D. Bouvard, M. Di Michiel, D. Bellet, G. Kapelski, Deformation of steel powder compacts during sintering: Correlation between macroscopic measurement and in situ microtomography analysis, Acta Mater 54 (2006) 513–522. https://doi.org/10.1016/j.actamat.2005.09.030.
[39] A. Cabo Rios, E. Hryha, E. Olevsky, P. Harlin, Sintering anisotropy of binder jetted 316L stainless steel: part II–microstructure evolution during sintering, Powder Metallurgy 0 (2021) 1–13. https://doi.org/10.1080/00325899.2021.2020486.
[40] S.-J.L. Kang, What We Should Consider for Full Densification when Sintering, Materials 13 (2020) 3578.
[41] S.A. McDonald, C. Holzner, E.M. Lauridsen, P. Reischig, A.P. Merkle, P.J. Withers, Microstructural evolution during sintering of copper particles studied by laboratory diffraction contrast tomography (LabDCT), Sci Rep 7 (2017) 1–11. https://doi.org/10.1038/s41598-017-04742-1.
[42] A. Vagnon, J.P. Rivière, J.M. Missiaen, D. Bellet, M. Di Michiel, C. Josserond, D. Bouvard, 3D statistical analysis of a copper powder sintering observed in situ by

synchrotron microtomography, Acta Mater 56 (2008) 1084–1093. https://doi.org/10.1016/j.actamat.2007.11.008.
[43] M.F. Ashby, A first report on deformation-mechanism maps, Acta Metallurgica 20 (1972) 887–897. https://doi.org/10.1016/0001-6160(72)90082-X.
[44] D.S. Wilkinson, M.F. Ashby, Pressure sintering by power law creep, Acta Metallurgica 23 (1975) 1277–1285. https://doi.org/10.1016/0001-6160(75)90136-4.
[45] Z.C. Cordero, B.E. Knight, C.A. Schuh, Six decades of the Hall–Petch effect – a survey of grain-size strengthening studies on pure metals, International Materials Reviews 61 (2016) 495–512. https://doi.org/10.1080/09506608.2016.1191808.
[46] B. Flipon, C. Keller, L.G. de la Cruz, E. Hug, F. Barbe, Tensile properties of spark plasma sintered AISI 316L stainless steel with unimodal and bimodal grain size distributions, Materials Science and Engineering: A 729 (2018) 249–256. https://doi.org/10.1016/j.msea.2018.05.064.
[47] E. Ma, Instabilities and ductility of nanocrystalline and ultrafine-grained metals, Scr Mater 49 (2003) 663–668. https://doi.org/10.1016/S1359-6462(03)00396-8.
[48] Coble, R. L. (1961). Sintering crystalline solids. i. Intermediate and final state diffusion models. Journal of Applied Physics, 32(5), 787–792. https://doi.org/10.1063/1.1736107.
[49] Oh, J. W., Ryu, S. K., Lee, W. S., & Park, S. J. (2017). Analysis of compaction and sintering behavior of 316L stainless steel nano/micro bimodal powder. Powder Technology (Print), 322, 1–8.
[50] Mirzababaei, S., & Pasebani, S. (2019). A review on Binder Jet additive manufacturing of 316L stainless steel. Journal of Manufacturing and Materials Processing, 3(3), 82. https://doi.org/10.3390/jmmp3030082
[51] Salas-Reyes, A. E., Qaban, A., & Mintz, B. (2024). Comments on the Intermediate-Temperature embrittlement of metals and alloys: The conditions for transgranular and intergranular failure. Metals, 14(3), 270. https://doi.org/10.3390/met14030270
[52] Zhang, Y., Quan, G., Zhao, J., Yu, Y., & Xiong, W. (2023). A Review on Controlling Grain Boundary Character Distribution during Twinning-Related Grain Boundary Engineering of Face-Centered Cubic Materials. Materials (Basel), 16(13), 4562. https://doi.org/10.3390/ma16134562
[53] Shveykin, A. I., Трусов, П. В., & Sharifullina, E. (2020). Statistical Crystal Plasticity Model Advanced for grain boundary sliding Description. Crystals, 10(9), 822. https://doi.org/10.3390/cryst10090822.
[54] Wang, *Hongtao, Sintering and Grain Growth of Nanosized Powder*, The University of Utah, 2010, [PhD Dissertation].